

## Extended Polyoxometalate Framework Solids: Two Mn(II)-Linked $\{P_8W_{48}\}$ Network Arrays

Scott G. Mitchell, Thomas Boyd, Haralampos N. Miras, De-Liang Long, and Leroy Cronin\*

*WestCHEM, School of Chemistry, The University of Glasgow, University Avenue, Glasgow, G12 8QQ, Scotland, U.K.*

Received July 22, 2010

Two polyoxometalate open framework (POMOF) materials have been synthesized using a secondary building unit (SBU) approach that facilitates the convergent assembly of multidimensional framework materials using a pre-assembled anionic SBU  $\{P_8W_{48}\}$ , with integrated “pore” 1 nm in diameter, and electrophilic manganese  $\{Mn^{2+}\}$  linkers. This yields two new POMOFs with augmented hexagonal tiling (**2** and **3**), related to a known three-dimensional (3D) cubic array  $K_{18}Li_6[Mn^{II}_8(H_2O)_{48}P_8W_{48}O_{184}] \cdot 108H_2O$  (**1**),  $K_{12}[Mn^{II}_{14}(H_2O)_{30}P_8W_{48}O_{184}] \cdot 111H_2O$  (**2**), and  $K_8Li_4[Mn^{II}_{14}(H_2O)_{26}P_8W_{48}O_{184}] \cdot 105H_2O$  (**3**). These frameworks have been crystallized from aqueous Li-buffered solutions of  $\{P_8W_{48}\}$  and  $Mn^{II}(ClO_4)_2 \cdot 6H_2O$  via careful control of the synthetic strategy akin to a crystal engineering approach using cation and temperature control to isolate different material architectures shown by compounds **1–3**.

### Introduction

Polyoxometalates (POMs) are an attractive and vast class of inorganic materials with a virtually unmatched range of physical and chemical properties<sup>1</sup> applicable to diverse areas of research such as catalysis,<sup>2</sup> medicine and biology,<sup>3</sup> magnetism,<sup>4</sup> and material science.<sup>5</sup> POMs cover an enormous range of size and structure<sup>6</sup> and thereby provide access to a huge library of readily available and controllable secondary building units (SBUs)<sup>7</sup> which can be interconnected by electrophilic linkers into interesting and functional architectures. Importantly,

this linker can be organic or inorganic in nature and as such POM-based materials are prime candidates for the design and construction of tailored molecular framework materials. In particular, the assembly of purely inorganic POM-based frameworks offers significant potential for the formation of new types of porous materials which combine the thermodynamic stability of zeolites<sup>8</sup> and mesoporous silicas with the sophistication and versatility of metal–organic frameworks (MOFs).<sup>9</sup> The accessible modularity of MOFs, specifically, the ability to modify the constituent component parts offers vast potential in modifying and controlling the properties of this class of materials. Respectively, the design and synthesis of cavity-containing and porous POMs is still in its infancy;<sup>10</sup> however, POMs offer a diverse class of materials with many applicable properties such as redox-switchability<sup>11</sup> and magnetism,<sup>4</sup> although most interestingly, several important reports show properties amenable particularly to catalysis and host–guest functionality.<sup>12</sup> Architectures built from all-inorganic molecular precursors such as these are of great interest and, importantly, many cyclic and “wheel-shaped” POM molecules

\*To whom correspondence should be addressed. E-mail: l.cronin@chem.gla.ac.uk. Homepage: <http://www.croninlab.com>. Fax: (+44)-141-330-4888.

(1) Long, D.-L.; Tsunashima, R.; Cronin, L. *Angew. Chem., Int. Ed.* **2010**, *49*, 1736.

(2) (a) Pluth, M. D.; Bergman, R. G.; Raymond, K. N. *Science* **2007**, *316*, 85. (b) Geletii, Y. V.; Besson, C.; Hou, Y.; Yin, Q.; Musaev, D. G.; Quiñero, D.; Cao, R.; Hardcastle, K. I.; Proust, A.; Kögerler, P.; Hill, C. L. *J. Am. Chem. Soc.* **2009**, *131*, 17360.

(3) (a) Shiget, S.; Mori, S.; Yamase, T.; Yamamoto, N.; Yamamoto, N. *Biomed. Pharmacother.* **2006**, *60*, 211. (b) Schemberg, J.; Schneider, K.; Demmer, U.; Warkentin, E.; Müller, A.; Ermler, U. *Angew. Chem., Int. Ed.* **2007**, *46*, 2408.

(4) (a) Ritchie, C.; Ferguson, A.; Nojiri, H.; Miras, H. N.; Song, Y.-F.; Long, D.-L.; Burkholder, E.; Murrie, M.; Kögerler, P.; Brechin, E. K.; Cronin, L. *Angew. Chem., Int. Ed.* **2008**, *47*, 5609. (b) Hussain, F.; Gable, R. W.; Speldrich, M.; Kögerler, P.; Boskovic, C. *Chem. Commun.* **2009**, 328. (c) Kögerler, P.; Tsukerblat, B.; Müller, A. *Dalton Trans.* **2010**, 39, 21.

(5) (a) AlDamen, M. A.; Cardona-Serra, S.; Clemente-Juan, J. M.; Coronado, E.; Gaita-Ariño, A.; Martí-Gastaldo, C.; Luis, F.; Montero, O. *Inorg. Chem.* **2009**, *48*, 3467. (b) Streb, C.; Long, D.-L.; Cronin, L. *Chem. Commun.* **2007**, 471.

(6) (a) Long, D.-L.; Cronin, L. *Chem.—Eur. J.* **2006**, *12*, 3698. (b) *Polyoxometalate Chemistry: From topology via self-assembly to applications*; Pope, M. T., Müller, A., Eds.; Kluwer: Dordrecht, The Netherlands, 2001.

(7) (a) Streb, C.; Ritchie, C.; Long, D.-L.; Kögerler, P.; Cronin, L. *Angew. Chem., Int. Ed.* **2007**, *46*, 7579. (b) Pradeep, C. P.; Long, D.-L.; Kögerler, P.; Cronin, L. *Chem. Commun.* **2007**, 41, 4254.

(8) Zeolites and ordered mesoporous materials: Progress and prospects. In *Studies in Surface Science*; van Bekkum, H., Cejka, J., Eds.; Elsevier: Amsterdam, The Netherlands, 2005; Vol. 157.

(9) Long, J. R.; Yaghi, O. M. *Chem. Soc. Rev.* **2009**, *38*, 1213.

(10) Marleny Rodríguez-Albelo, L.; Ruiz-Salvador, R.; Sampieri, A.; Lewis, D. W.; Gómez, A.; Nohra, B.; Mialane, P.; Marrot, J.; Sécheresse, F.; Mellot-Draznieks, C.; Ngo Biboum, R.; Keita, B.; Nadjo, L.; Dolbecq, A. *J. Am. Chem. Soc.* **2009**, *131*, 16078.

(11) (a) Ritchie, C.; Streb, C.; Thiel, J.; Mitchell, S. G.; Miras, H. N.; Long, D.-L.; Boyd, T.; Peacock, R. D.; McGlone, T.; Cronin, L. *Angew. Chem., Int. Ed.* **2008**, *47*, 6881. (b) Thiel, J.; Ritchie, C.; Streb, C.; Long, D.-L.; Cronin, L. *J. Am. Chem. Soc.* **2009**, *131*, 4180.

(12) Mitchell, S. G.; Streb, C.; Miras, H. N.; Boyd, T.; Long, D.-L.; Cronin, L. *Nat. Chem.* **2010**, *2*, 308.

can be synthesized, thereby offering the possibility of designing frameworks with integrated pores. Although the careful control of reaction conditions is most commonly used to encourage coordination bond interactions between discrete POM units, this approach has clear limitations owing to the complex self-assembly nature of POM compounds. This has stimulated us to exploit the use of specific POM clusters which can function effectively as SBUs and study their tendency to aggregate into interesting molecular assemblies. Our investigations have shown that by using this approach the construction of intricate three-dimensional (3D) frameworks is in fact possible.<sup>12</sup>

We chose to employ the superlacunary crown-type  $[P_8W_{48}O_{184}]^{40-}$  polyanion<sup>13</sup> (herein  $\{P_8W_{48}\}$ ) as an SBU, a model component part for several reasons. The majority of the recent  $\{P_8W_{48}\}$ -based crown HPAs encapsulate various transition metal and alkali metal ions in the central crown cavity, of diameter about 1 nm. The substitution within this “pore” cavity is assisted by the flexibility of the polyanion with regard to incoming guest species. There are numerous recent literature examples: from the copper-containing  $[Cu_{20}Cl(OH)_{24}(H_2O)_{12}(P_8W_{48}O_{184})]^{25-14}$  and other transition metal-containing clusters,<sup>15</sup> to  $[K_8C\{P_8W_{48}O_{184}\}\{V_4V^{IV}O_{12}(H_2O)_2\}_2]$  aggregates,<sup>16</sup> organoruthenium-based composites<sup>17</sup> and framework architectures.<sup>18</sup> Imperative in the current design context, however, is the ability of the  $\{P_8W_{48}\}$  polyanion to extend into multidimensional architectures by electrophilic functionalization of the outer sphere, as opposed to the internal cavity.<sup>18</sup> Indeed, we have recently shown that this approach is possible by the assembly of an infinite nanocube array whereby each nanocube comprises six coordinated  $\{P_8W_{48}\}$  polyanion units which are linked via exo Mn coordinated linkers to yield  $K_{18}Li_6[Mn^{II}_8(H_2O)_{48}P_8W_{48}O_{184}] \cdot 108H_2O$  (**1**).<sup>12</sup> The highly anionic crown-type POM,  $\{P_8W_{48}\}^{40-}$ , which incorporates a 1 nm pore, functions as a primary SBU that, when combined with redox-switchable electrophilic Mn(II) cation linkers, can form accessible open framework architectures. The work reported herein expands this initial discovery showing the design and synthetic approach that allows the assembly of two additional infinite framework materials that have been designed from  $\{P_8W_{48}\}$ : a model POM molecular building block. The structural exploitation of the  $\{P_8W_{48}\}$  polyoxoanion and its assembly into two 3D POM frameworks with intriguing topologies, comparable to that of zeolites and related compounds, gives great promise to the use of these all-inorganic frameworks as functional materials.  $K_{12}[Mn^{II}_{14}(H_2O)_{30}P_8W_{48}O_{184}] \cdot 111H_2O$  (**2**) and  $K_8Li_4[Mn^{II}_{14}(H_2O)_{26}P_8W_{48}O_{184}] \cdot 105H_2O$  (**3**) have been crystallized from aqueous Li-buffered solutions of  $\{P_8W_{48}\}$  and  $Mn^{II}(ClO_4)_2 \cdot 6H_2O$  via careful control of the synthetic strategy akin to a crystal engineering approach.

## Results and Discussion

To synthesize a material which functions effectively we require a level of predictability in its formation. Indeed it is

not only the building blocks that are important, but the way in which they are connected, thus careful experimental design can control the formation of desired architectures. We surmised that the highly anionic  $\{P_8W_{48}\}$  cluster could form the basis of a molecular scaffold to effectively yield new high nuclearity arrangements with integrated porous apertures. This highly stable and versatile  $[P_8W_{48}O_{184}]^{40-}$  ring-shaped cluster is in fact an oligomer formed from the linking of four subunits of the hexavacant  $[\alpha-H_2P_2W_{12}O_{48}]^{12-}$  polyoxoanion. These vacant subunits are, in turn, derived from the phosphotungstate Dawson-type anion  $[\alpha-P_2W_{18}O_{62}]^{6-}$ . The simple one-pot syntheses reported herein were designed based on previous experimental observations, from the original  $\{P_8W_{48}\}$  paper and subsequent investigations.<sup>12,13</sup> One vital key toward the successful synthesis of the 48-tungstophosphate materials appears to be precisely buffered mildly acidic aqueous media, although other factors also appear to be crucial to the formation of multidimensional architectures in preference to discrete functionalized  $\{P_8W_{48}\}$  motifs. Several studies now demonstrate the degree of sensitivity of the POM self-assembly process, highlighting the importance of pH value, ionic strength, temperature and reagent type and ratios in the synthesis of novel structures.<sup>14</sup> This led us to investigate how minor modifications of the reaction conditions would affect the synthesis of network structures related to our recently published nanocube-based framework material  $K_{18}Li_6[Mn^{II}_8(H_2O)_{48}P_8W_{48}O_{184}] \cdot 108H_2O$  (**1**).<sup>12</sup> Although compounds  $K_{12}[Mn^{II}_{14}(H_2O)_{30}P_8W_{48}O_{184}] \cdot 111H_2O$  (**2**) and  $K_8Li_4[Mn^{II}_{14}(H_2O)_{26}P_8W_{48}O_{184}] \cdot 105H_2O$  (**3**) share identical building blocks to this nanocube-based material, the resulting topologies of these architectures are quite different (see Figure 1).

Compound **1** has been described previously<sup>12</sup> and was crystallized from aqueous LiOAc-buffered solution (pH 4.0) following reaction of  $\{P_8W_{48}\}$  with  $Mn^{II}(ClO_4)_2 \cdot 6H_2O$  at 80 °C. Reported in this article, compounds  $K_{12}[Mn^{II}_{14}(H_2O)_{30}P_8W_{48}O_{184}] \cdot 111H_2O$  (**2**) and  $K_8Li_4[Mn^{II}_{14}(H_2O)_{26}P_8W_{48}O_{184}] \cdot 105H_2O$  (**3**) have been crystallized from mildly acidic and dilute aqueous LiCl-buffered solutions of  $\{P_8W_{48}\}$  and  $Mn^{II}(ClO_4)_2 \cdot 6H_2O$ . These compounds have been fully characterized by single crystal X-ray crystallography, powder X-ray diffraction (PXRD), cyclic voltammetry (CV), thermogravimetric analysis (TGA), flame photometry (FP) as well as flame atomic absorption spectroscopy (FAAS), FT-IR, and UV-vis spectroscopy (Figure 2, Table 1). Consequently, crystal engineering experimental procedures were adopted for the syntheses of compounds **2** and **3**. The pH of aqueous 2 M LiCl solution required the addition of just one drop of acetic acid to reach exactly pH 4.0; and to this stirring solution was added manganese(II) perchlorate, followed by the cyclic HPA SBU  $\{P_8W_{48}\}$ . These components were reacted overnight by vigorously stirring the solutions and, upon standing, at a temperature constantly maintained at 19 °C; the solutions began the crystallization process approximately one to two weeks thereafter. In both cases, **2** and **3** were the only products crystallized from solution, and the only altered experimental variable was the temperature of overnight reaction; specifically room temperature (ca. 20 °C) for **2**; and 80 °C for **3**, all other variables were maintained as constant.

(13) Contant, R.; Tézé, A. *Inorg. Chem.* **1985**, *24*, 4610.

(14) Mal, S. S.; Kortz, U. *Angew. Chem., Int. Ed.* **2005**, *44*, 3777.

(15) Bassil, B. S.; Ibrahim, M.; Sankar Mal, S.; Suchopar, A.; Ngo Biboum, R.; Keita, B.; Nadjio, L.; Nellutla, S.; van Tol, J.; Dalal, N. S.; Kortz, U. *Inorg. Chem.* **2010**, *49*, 4949.

(16) Müller, A.; Pope, M. T.; Todea, A. M.; Bögge, H.; van Slageren, J.; Dressel, M.; Gouzerh, P.; Thouvenot, R.; Tsukerblat, B.; Bell, A. *Angew. Chem., Int. Ed.* **2007**, *46*, 4477.

(17) Mal, S. S.; Nsouli, N. H.; Dickman, M. H.; Kortz, U. *Dalton Trans.* **2007**, 2627.

(18) Mitchell, S. G.; Gabb, D.; Ritchie, C.; Hazel, N.; Long, D.-L.; Cronin, L. *CrystEngComm* **2009**, *11*, 36.

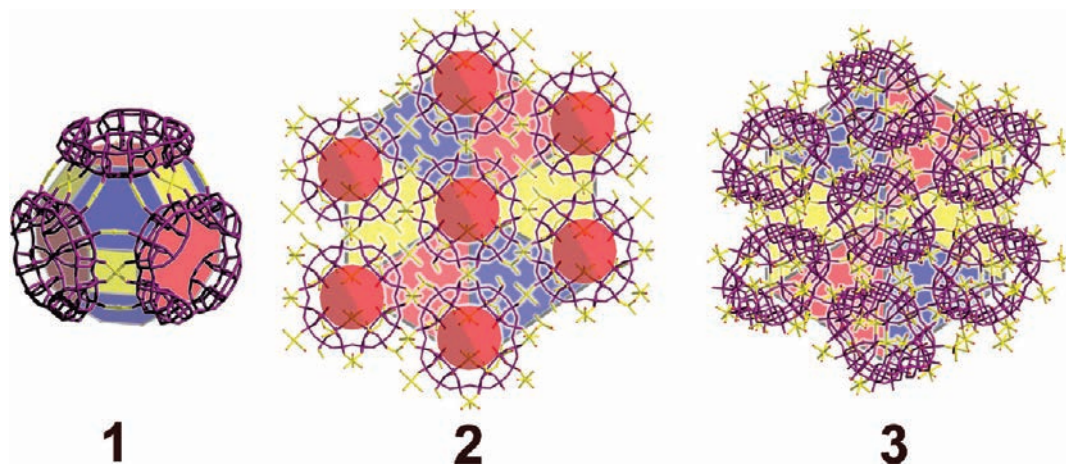


**Figure 1.** Comparison of the three manganese-linked  $\{P_8W_{48}\}$  framework compounds: Nanocube-based framework material  $K_{18}Li_6[Mn^{II}_8(H_2O)_{48}P_8W_{48}O_{184}] \cdot 108H_2O$  (**1**)<sup>12</sup> showing the packing of  $\{P_8W_{48}\}$  building units around a *truncated cuboctahedron*; compound  $K_{12}[Mn^{II}_{14}(H_2O)_{30}P_8W_{48}O_{184}] \cdot 111H_2O$  (**2**) viewed along the crystallographic *b* axis where large red spheres represent the “pore” channels through this axis. For **2** and **3**, the underlying hexagons provide an illustration of the approximate hexagonal close packing of  $\{P_8W_{48}\}$  fragments within discrete  $\{P_8W_{48}\}$  layers. Purple bonds, W–O; small red spheres, oxygen; yellow bonds, Mn–O. All cations and solvent water molecules have been omitted for clarity.

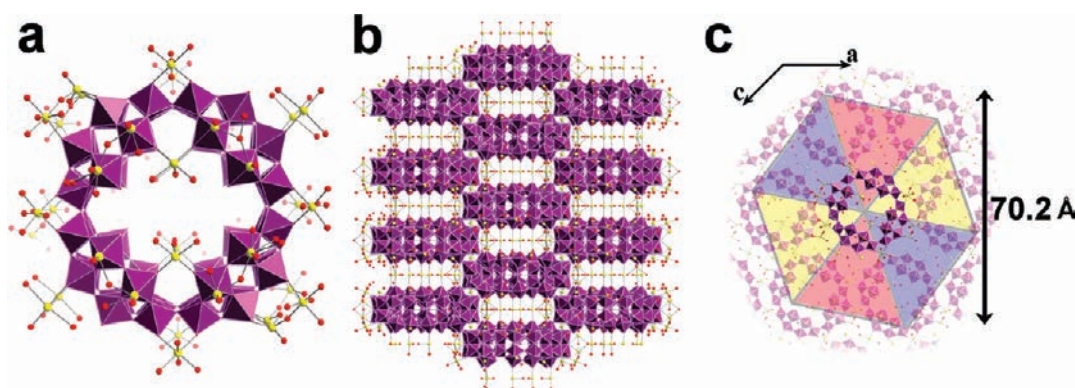


**Figure 2.** (a)  $[Mn^{II}_{14}(H_2O)_{30}P_8W_{48}O_{184}]^{12-}$  (**2a**); (b) view along the crystallographic *c* axis illustrating layers of  $\{P_8W_{48}\}$  units; (c) detailed illustration of the approximate hexagonal close packing of  $\{P_8W_{48}\}$  fragments as viewed along the crystallographic *b* axis showing large cylindrical channels, provided by the HPA SBU  $\{P_8W_{48}\}$ . Purple polyhedra,  $WO_6$ ; red spheres, oxygen; yellow spheres, Mn. All cations and solvent water molecules have been omitted for clarity.

Crystals obtained by slow open-flask evaporation methods over the period of about one month were perfectly suitable for single crystal X-ray diffraction analysis; however, high quality single crystals may also be obtained by vapor diffusion of a suitable solvent such as methanol into the mother liquor. The synthetic procedures presented here are entirely reproducible although we have found that crystallization times may vary by several days from batch to batch, despite the crystallization room temperature being maintained at 19 °C.

All three compounds can be considered as 3D networks based on the  $\{Mn-O-W\}$  coordination bonds between discrete  $\{P_8W_{48}\}$  fragments. It is, however, the number and location of Mn(II) centers on each  $\{P_8W_{48}\}$  unit that seems to dictate the arrangement of the cyclic  $\{P_8W_{48}\}$  in the crystal lattice. The packing of these anions within the frameworks of **1** and **2** are highly ordered although compound **3**, by comparison, is somewhat more disordered.

Compound  $K_{12}[Mn^{II}_{14}(H_2O)_{30}P_8W_{48}O_{184}] \cdot 111H_2O$  (**2**) can be viewed as a 3D framework of rigid porous cylinders resulting from the cooperation between the POM/Mn ion moieties in combination with alkali metals and solvent water molecules (Figure 3). The cylinders adopt approximate

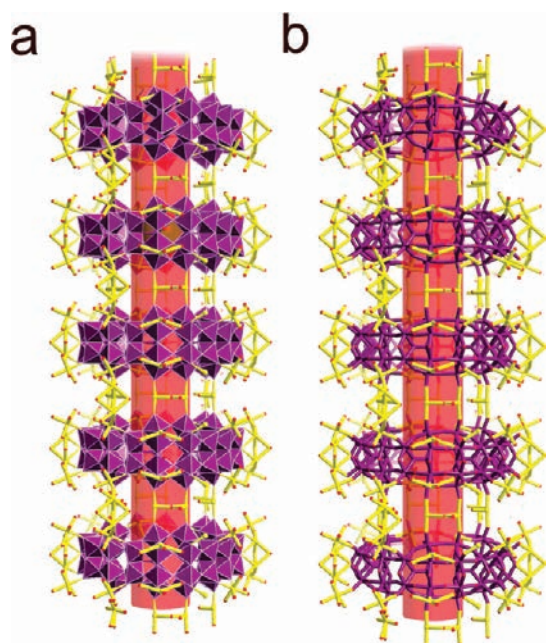
hexagonal packing along the crystallographic *b*-axis leading to an architecture with distinct pore windows of dimension about 10.75 Å in diameter, of course relating to the crown cavity of the  $\{P_8W_{48}\}$  fragment. Each  $\{P_8W_{48}\}$  molecule contains 2 Mn(II) ions in the crown cavity, effectively reducing its size, as well as a further 12 located on the outside edge. Extension of the  $\{Mn-O-W\}$  coordination bonding describes a well-ordered network whereby the cyclic  $\{P_8W_{48}\}$  units are layered directly on top of one another with respect to the crystallographic *b* axis but staggered along the *c* axis. TGA analysis has shown that the thermal decomposition profile of the material follows a characteristic POM format, albeit cluster decomposition occurs at elevated temperatures. Approximately 12% of the weight of compound **2** is lost over the first 200 °C, which is attributed to loss of solvent and coordinated water molecules; followed by cluster collapse beginning at 400 °C.

During these investigations, many reaction conditions were scanned and explored; however, it was found that, following introduction of all the necessary starting materials, by simply heating the reaction mixture to 80 °C, a distorted analogue of **2** is formed. Heating the reaction mixture appears to cause a distortion in the forming 3D architecture relating to the

**Table 1.** Crystal Data and Structure Refinement for  $K_{12}[Mn^{II}_{14}(H_2O)_{30}P_8W_{48}O_{184}] \cdot 111H_2O$  (**2**) and  $K_8Li_4[Mn^{II}_{14}(H_2O)_{26}P_8W_{48}O_{184}] \cdot 105H_2O$  (**3**)

	<b>2</b>	<b>3</b>
empirical formula	$H_{282}K_{12}Mn_{14}O_{325}P_8W_{48}$	$H_{262}K_8Li_4Mn_{14}O_{315}P_8W_{48}$
$F_w$ (g mol <sup>-1</sup> )	15794.46	15485.68
wavelength (Å)	0.71073 (Mo $K_{\alpha}$ )	0.71073 (Mo $K_{\alpha}$ )
crystal size (mm)	0.14 × 0.11 × 0.05	0.28 × 0.24 × 0.05
crystal system	monoclinic	monoclinic
space group	$C2/m$	$P2_1/c$
$a$ (Å)	45.766(3)	17.8226(2)
$b$ (Å)	14.3753(8)	20.2260(2)
$c$ (Å)	26.618(3)	37.2304(6)
$\beta$ (deg)	123.916(5)	100.219(12)
$V$ (Å <sup>3</sup> )	14532.1(19)	13207.9(3)
$Z$	2	2
$\rho_{\text{calcd}}$ (g cm <sup>-3</sup> )	3.610	3.894
$\mu$ (mm <sup>-1</sup> )	19.84	21.76
$T$ (K)	150(2)	150(2)
absorption correction	analytical	analytical
goodness-of-fit on $F^2$	1.163	1.053
no. of reflections (measured)	46196	58925
no. of reflections (unique)	13716	23984
$R_{\text{int}}$	0.1352	0.0566
unique observed reflections [ $I > 2\sigma(I)$ ]	8909	16456
final $R$ indices: $R_{1(\text{obs})}$ ; $wR_{2(\text{all data})}^a$	0.1251; 0.3403	0.0534; 0.1211

$$^a R_1 = \sum ||F_o| - |F_c|| / \sum |F_o|; wR_2 = [\sum w(F_o^2 - F_c^2)^2 / \sum w(F_o^2)^2]^{1/2}.$$

**Figure 3.**  $\{P_8W_{48}\}$  cluster arrangement forming cylindrical pores of **2** through the crystallographic  $b$  axis which extends into an augmented hexagonal 3D network. (a) polyhedral representation; (b) wire representation, where red cylinder is a vector representing the “pore” channels along the crystallographic  $b$ -axis.

$\{W-O-Mn\}$  coordination sites on the  $\{P_8W_{48}\}$  SBU—compound **3** is the result (Figure 4). The internal crown cavity size and other relevant dimensions of the  $\{P_8W_{48}\}$  are near identical; for example, the diameter of the cavity measures 10.71 Å and the binding angles of the  $\{P_2W_{12}\}$  fragments are closely related (see Supporting Information, Table S1 for further details). However, the Mn cations are disordered over several sites in the cavity thereby reducing its size. The TGA profile of **3** also shows similar features to that of **2**; most notably, about 12% of the weight of compound is lost over the first 200 °C, attributed to loss of solvent and coordinated water molecules; followed by cluster collapse beginning at 400 °C.

For compounds **1–3**, the intramolecular bonding between  $\{P_8W_{48}\}$  subunits leads to a complex connectivity pattern, but the structural features can be simplified by rationalizing the  $\{W-O-Mn\}$  bonding between fragments; specifically, it is the location of the Mn ions on the  $\{P_8W_{48}\}$  cluster which give rise to such varied structures. In compounds **2** and **3**, the two apical W atoms from each end of the  $\{P_2W_{12}\}$  fragment are involved in bonding to neighboring units to form the  $\{P_8W_{48}\}$  ring, however, one terminal  $W=O$  remains free for electrophilic addition. In all cases, this is a prime site for a Mn ion to bind, bridging between two  $\{P_2W_{12}\}$  fragments. Similarly, the equatorial W sites, which lie *trans* to the apical W positions, both contain  $\{W-O-Mn\}$  bonds. Most importantly, however, the presence of Mn ions on the equatorial (belt region) W atom sites, which lie facing out of the plane of the ring at 90°, appear to be crucial for the well-defined columnar packing of  $\{P_8W_{48}\}$  units seen in **2**. Curiously, it is precisely the absence of Mn ions on these W sites which give rise to the cubic packing observed in a previously reported Mn-substituted nanocube-based compound,  $K_{18}Li_6[Mn^{II}_8(H_2O)_{48}P_8W_{48}O_{184}] \cdot 108H_2O$  (**1**).<sup>12</sup>

The redox behavior of compound **2** has been studied in aqueous solution. Figure 5 shows the main characteristic peaks associated with W and Mn redox couples of **2** between +2.000 V and -1.100 V versus Ag/AgCl at the scan rate region of 100 mV/s. The form of the diagram remained identical irrespective of the direction of the scanning potential. At the aforementioned scan rate, and scanning toward the negative region of potential values, the reduction of W centers occurred through three separated steps, with the corresponding  $E_{1/2}$  peak potentials located respectively at -0.404, -0.630, and -0.939 V (vs Ag/AgCl).<sup>19,20</sup> At the positive region of potential values two quasi-irreversible oxidation peaks observed with the  $E_{1/2}$  peak potentials to be located at

(19) Mitchell, S. G.; Khanra, S.; Miras, H. N.; Boyd, T.; Long, D.-L.; Cronin, L. *Chem. Commun.* **2009**, 2712.

(20) (a) Bi, L. H.; Wang, E.-B.; Peng, J.; Huang, R. D.; Xu, L.; Hu, C. W. *Inorg. Chem.* **2000**, 39, 671. (b) Mbomekalle, I. M.; Keita, B.; Nadjo, L.; Berthet, P.; Neiwert, W. A.; Hill, C. L.; Ritorto, M. D.; Anderson, T. M. *Dalton Trans.* **2003**, 2646.

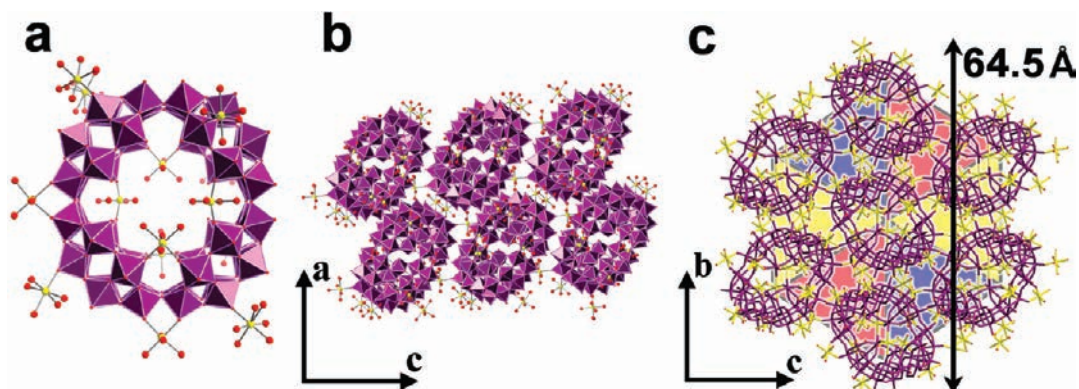


**Figure 4.** (a)  $[\text{Mn}^{\text{II}}_{14}(\text{H}_2\text{O})_{26}\text{P}_8\text{W}_{48}\text{O}_{184}]^{12-}$  (**3a**); (b) view along the crystallographic  $b$  axis illustrating layers of  $\{\text{P}_8\text{W}_{48}\}$  units; (c) detailed illustration of the distorted hexagonal close packing of  $\{\text{P}_8\text{W}_{48}\}$  fragments as viewed along the crystallographic  $a$  axis. Purple polyhedra:  $\text{WO}_6$ ; Red spheres, oxygen; yellow spheres, Mn. All cations and solvent water molecules have been omitted for clarity.

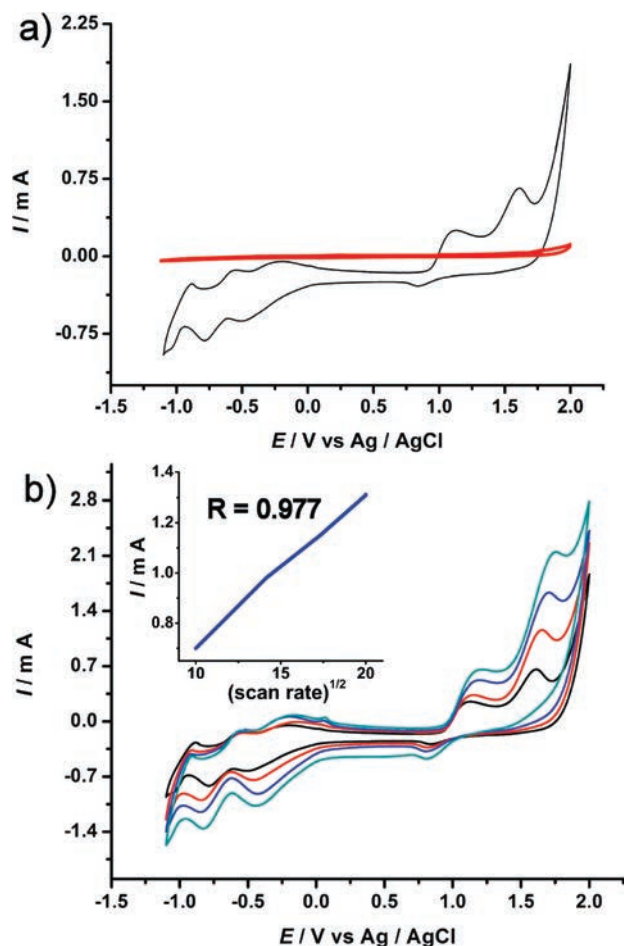


**Figure 5.** Cyclic voltammograms of **2**: (a) in the potential region of  $-1100$  to  $+2000$  mV at a scan rate of  $100$  mV/s, where red line represents a plot of the blank buffer solution; (b) at scan rates (from inner to outer)  $100$ ,  $200$ ,  $300$ , and  $400$  mV/s. Concentration of **2** was  $2 \times 10^{-3}$  M in  $10$  mL of  $\text{CH}_3\text{COONa}$ :  $0.2$  M  $\text{Na}_2\text{SO}_4$  buffer solution, the working electrode was glassy carbon ( $3$  mm) and the reference electrode was  $\text{Ag}/\text{AgCl}$ . Inset: Representation of the current as a function of the square root of the scan rate.

$+0.980$  and  $+1.635$ . In the first instance we therefore observed the simultaneous oxidation of all  $\text{Mn}(\text{II})$  centers,

followed thereafter by an oxidation from  $\text{Mn}(\text{III})$  to  $\text{Mn}(\text{IV})$ . The characteristic sharpness of the oxidation wave is indicative of the presence of a surface-active species.<sup>21</sup> The cyclic voltammograms of compound **2** at different scan rates are also represented in Figure 5. The peak currents were proportional to the scan rate, indicating that the redox process of **2** is surface-controlled when the scan rate does not exceed the rate of  $50$  mV/s. Above  $100$  mV/s the peak currents were proportional to the square root of the scan rate, suggesting that redox process is diffusion-controlled. Broadening and overlapping of the redox couples takes place as soon as the scan rate exceeds the value of  $100$  mV/s and as a consequence, important redox-related information is concealed.

The redox behavior of compound **3** was studied in the same medium under the same conditions and is presented in Figure 6. Scanning toward the negative region of potential were observed three reversible W-centered redox couples with the corresponding  $E_{1/2}$  peak potentials located respectively at  $-0.055$ ,  $-0.341$ , and  $-0.642$  V (vs  $\text{Ag}/\text{AgCl}$ ).<sup>19,20</sup> At the positive region of potential values a quasi-reversible and an irreversible oxidation peak observed with the  $E_{1/2}$  peak potentials to be located at  $+1.269$  and  $+1.989$  V respectively. The simultaneous oxidation of all  $\text{Mn}(\text{II})$  centers can be observed also in this case, followed by an oxidation from  $\text{Mn}(\text{III})$  centers to  $\text{Mn}(\text{IV})$  accompanied by the absorption of active species on the surface of the electrode.<sup>21</sup> Various cases were described in the literature for the oxidation pathways of Mn centers within POMs, with a variety of situations, including important differences in potential locations.<sup>22</sup> Furthermore, Figure 6 also includes the cyclic voltammograms of **3** at different scan rates. The variation of the peak current intensity as a function of the square root of the scan rate indicates that the voltammograms feature a diffusion-controlled process.

Comparison of the electrochemical behavior of compounds **2** and **3** shows that similar processes are taking place, as may very well be expected. Interestingly, the presence of the  $\text{Mn}(\text{II})$  centers has little influence on the redox characteristics associated with the  $\text{W}(\text{VI})$  centers in the case of compound **2**. When comparing with the corresponding W-waves of the discrete  $\{\text{P}_8\text{W}_{48}\}$  ring, the main W-reduction couples of **2** undergo a significant shift in the negative

(21) Liw, J.; Ortega, F.; Sethuraman, P.; Katsoulis, D. E.; Costello, C. E.; Pope, M. T. *J. Chem. Soc., Dalton Trans.* **1992**, 1901.

(22) (a) Bosing, M.; Noh, A.; Loose, I.; Krebs, B. *J. Am. Chem. Soc.* **1998**, *120*, 7252. (b) Keita, B.; Mbomekalle, I. M.; Lu, Y. W.; Nadjjo, L.; Berthet, P.; Anderson, T. M.; Hill, C. L. *Eur. J. Inorg. Chem.* **2004**, 3462.

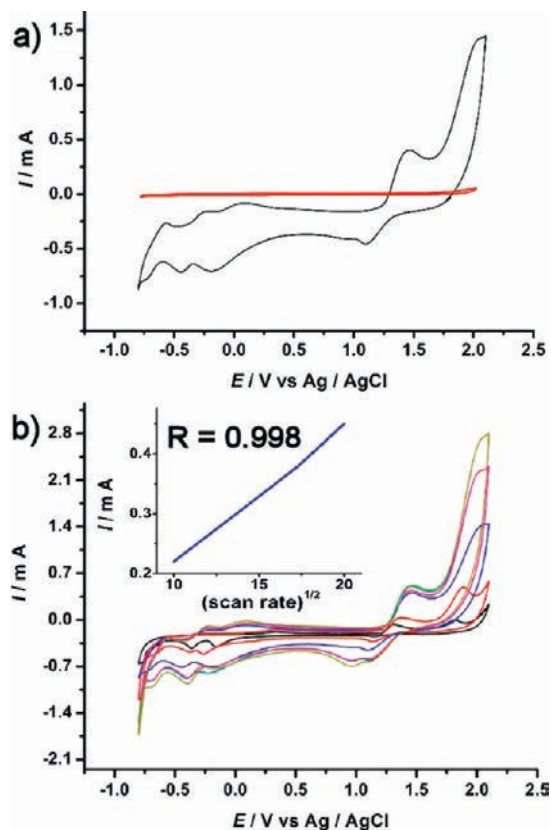


**Figure 6.** Cyclic voltammograms of **3**: (a) in the potential region of  $-1100$  to  $+2000$  mV at a scan rate of  $100$  mV/s, where the red line represents a plot of the blank buffer solution; (b) at scan rates (from inner to outer)  $100$ ,  $200$ ,  $300$ , and  $400$  mV/s. Concentration of **3** was  $2 \times 10^{-3}$  M in  $10$  mL of  $\text{CH}_3\text{COONa}$ :  $0.2$  M  $\text{Na}_2\text{SO}_4$  buffer solution, the working electrode was glassy carbon ( $3$  mm) and the reference electrode was Ag/AgCl. Inset: Representation of the current as a function of the square root of the scan rate.

potential direction. From a strictly electrostatic point of view, a shift of these waves toward the positive potential direction may have been expected, since the overall negative charge of **2** is lower than that of  $\{\text{P}_8\text{W}_{48}\}$ , because of the presence of  $14$  manganese centers around the ring. On the contrary, compound **3** revealed a shift of the three redox couples toward the positive region of potentials according to our prediction. Therefore, the interaction of the Mn(II)-bridges connecting discrete  $\{\text{P}_8\text{W}_{48}\}$  moieties into the extended architecture must exert a direct, but minor, influence on the electrochemical properties. Although the redox characteristics of the W(VI) centers alone cannot be used as a method of evaluation of the extent of interaction between the Mn(II) centers and the  $\{\text{P}_8\text{W}_{48}\}$  unit, we can also attribute these rather large redox couple shifts to the minor differences in connectivity of Mn(II) centers on each  $\{\text{P}_8\text{W}_{48}\}$  fragments in **2** and **3**. Since all experimental variables are kept constant, these effects require more understanding and are currently under investigation.

Another noteworthy feature of these electrochemistry studies is that in the case of compound **3** the W- and Mn-centered processes are affected differently as a function of the scan rate. Perhaps the connectivity of the  $\{\text{P}_8\text{W}_{48}\}$  clusters through manganese centers influences the rate of the electron-transfer processes in a completely contradictory fashion. At slow scan rates ( $< 50$  mV/s) the Mn-centered redox waves were more clearly defined; while increasing the scan

rate shifted these waves rapidly to more positive potential values. Consequently, the peak separation increases and the processes become ill-defined while it approaches the discharge limit of the solvent. On the contrary, the W-related redox processes become (quasi-)reversible at scan rates higher than  $50$  mV/s. In addition, the same processes in the case of compound **2** appear to be affected in a similar way. Upon increase of the scan rate, the peak separation increases accordingly, but the W-centered redox couples retained their (quasi-)reversible nature (Figure 5). The structure-induced electronic communication between the  $\{\text{P}_8\text{W}_{48}\}$  “synthons” of the architecture is a very interesting point which requires an extensive study using more informative techniques than electrochemistry. Experiments are under way and will be reported in due course.

## Conclusions

In conclusion, we were able to obtain two closely related yet highly distinctive novel hetero-POM framework materials based on a highly anionic secondary POM building unit,  $\{\text{P}_8\text{W}_{48}\}^{40-}$ , in combination with  $\{\text{Mn}\}^{2+}$  linkers. This expands on our previous work on  $\{\text{P}_8\text{W}_{48}\}^{40-}$  and  $\{\text{Co}\}^{2+}$  linkers where we succeeded in isolating  $1\text{D}$  chains and  $2\text{D}$  networks and also our previous work with  $\{\text{Mn}\}^{2+}$  linkers which resulted in a  $3\text{D}$  nanocube-based framework architecture (**1**). Importantly, the integrated and accessible channels provided by the crown cavity of  $\{\text{P}_8\text{W}_{48}\}$  lead to well-defined sizable channels into which small molecules can be absorbed.<sup>12</sup> Compound **2** contains microporous channels leading to topology analogous to that of zeolites and other framework materials; however, loss of solvent water molecules through dehydration causes the materials to lose their single crystalline nature and, consequently, their functionality. It is noteworthy that the network arrays  $\text{K}_{18}\text{Li}_6[\text{Mn}^{II}_8(\text{H}_2\text{O})_{48}\text{P}_8\text{W}_{48}\text{O}_{184}] \cdot 108\text{H}_2\text{O}$  (**1**),<sup>12</sup>  $\text{K}_{12}[\text{Mn}^{II}_{14}(\text{H}_2\text{O})_{30}\text{P}_8\text{W}_{48}\text{O}_{184}] \cdot 111\text{H}_2\text{O}$  (**2**), and  $\text{K}_8\text{Li}_4[\text{Mn}^{II}_{14}(\text{H}_2\text{O})_{26}\text{P}_8\text{W}_{48}\text{O}_{184}] \cdot 105\text{H}_2\text{O}$  (**3**) represent some of the first examples whereby  $\{\text{P}_8\text{W}_{48}\}$  has been extended into coordination bonded assemblies with long-range crystalline order (see Scheme 1).

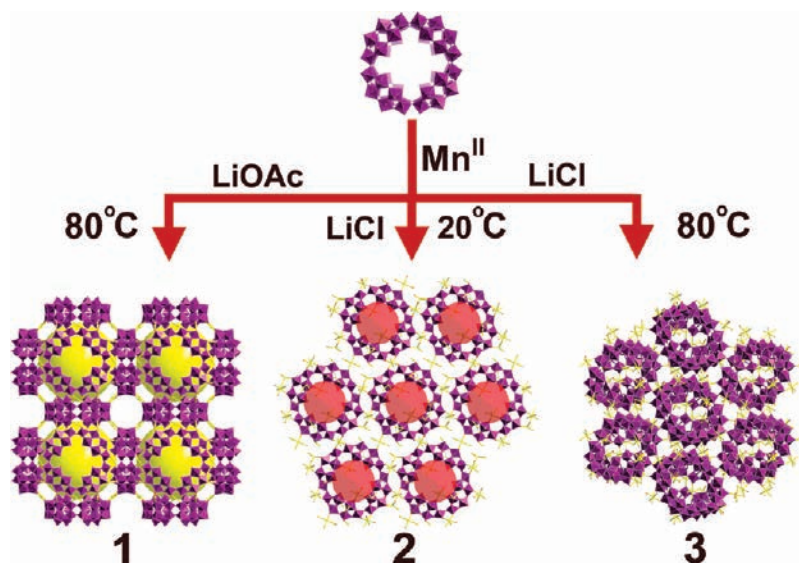
This discovery takes POM research one step away from discovery-based synthetic chemistry with a move toward linking together functional building blocks which will exhibit a desired chemical property. Further studies will investigate the catalytic functionality and sorption capabilities of **2** and **3** in detail and as well as extending these synthetic approaches to further-develop and tailor the chemical properties of this class of materials.

## Experimental Section

**Materials.** All chemicals and solvents were of analytical grade purchased from Sigma Aldrich and used as supplied, without further purification.  $\text{K}_{28}\text{Li}_5[\text{H}_7\text{P}_8\text{W}_{48}\text{O}_{184}] \cdot 92\text{H}_2\text{O}$  was synthesized from a modified method adapted from the original  $\{\text{P}_8\text{W}_{48}\}$  paper published by Contant and Tézé.<sup>13</sup> Synthesis, characterization, and discussion of  $\text{K}_{18}\text{Li}_6[\text{Mn}^{II}_8(\text{H}_2\text{O})_{48}\text{P}_8\text{W}_{48}\text{O}_{184}] \cdot 108\text{H}_2\text{O}$  (**1**) has been reported elsewhere.<sup>12</sup>

**Synthesis.**  $\text{K}_{12}[\text{Mn}^{II}_{14}(\text{H}_2\text{O})_{30}\text{P}_8\text{W}_{48}\text{O}_{184}] \cdot 111\text{H}_2\text{O}$  (**2**). The pH of a  $15$  mL solution of  $1$  M LiCl solution was adjusted to exactly  $4.0$  by addition of one drop of  $1$  M acetic acid solution. To this solution was then added successively  $\text{Mn}(\text{ClO}_4)_2 \cdot 6\text{H}_2\text{O}$  ( $102$  mg,  $0.28$  mmol) and  $\text{K}_{28}\text{Li}_5[\text{H}_7\text{P}_8\text{W}_{48}\text{O}_{184}] \cdot 92\text{H}_2\text{O}$  ( $100$  mg,  $6.8$   $\mu\text{mol}$ ). The near colorless mixture was stirred at room temperature (ca.  $20$   $^\circ\text{C}$ ) overnight (approximately  $20$  h), whereupon it

**Scheme 1.** Representation of the Synthetic Procedures Used to Isolate  $K_{18}Li_6[Mn^{II}_8(H_2O)_{48}P_8W_{48}O_{184}] \cdot 108H_2O$  (**1**)<sup>12</sup> and Compounds  $K_{12}[Mn^{II}_{14}(H_2O)_{30}P_8W_{48}O_{184}] \cdot 111H_2O$  (**2**) and  $K_8Li_4[Mn^{II}_{14}(H_2O)_{26}P_8W_{48}O_{184}] \cdot 105H_2O$  (**3**)<sup>a</sup>



<sup>a</sup>  $\{P_8W_{48}\}$  is used in combination with manganese(II) perchlorate at pH 4.0 where only the reaction temperature (20 or 80 °C) and solvent system (aqueous 2M lithium acetate or lithium chloride) are varied. Purple polyhedra,  $WO_6$ ; Red spheres, oxygen; yellow spheres, Mn. All cations and solvent water molecules have been omitted for clarity. Yellow spheres represent the approximately spherical void space (ca. 7.24 nm<sup>3</sup>) within the cavity of each cuboctahedral building unit of  $K_{18}Li_6[Mn^{II}_8(H_2O)_{48}P_8W_{48}O_{184}] \cdot 108H_2O$  (**1**); while the large red spheres represent the columnar channels present in **2**.

turned from almost colorless to pale yellow, and transferred to a glass vial. After one week of crystallizing at constant temperature (19 °C), pale yellow rectangular plate crystals formed in solution. These were separated 7 days after crystallization began. Diffraction quality crystals were grown by the slow diffusion of methanol into the reaction mother liquor. Yield = 33 mg, 2.0 μmol, 31% based on W.

It should be noted that 2 M LiCl was originally employed for the synthesis of **2**, but the quality of single crystals can be improved by using 1 M LiCl.

Elemental analysis for  $K_{12}[Mn^{II}_{14}(H_2O)_{30}P_8W_{48}O_{184}] \cdot 108H_2O$ ,  $H_{276}K_{12}Mn_{14}O_{322}P_8W_{48}$  (**2**), MW = 15794.47 g mol<sup>-1</sup>. Calculated values (found values in brackets): Mn 4.87 (4.67), W 55.87 (55.81), K 2.97 (2.65) %.<sup>23</sup> TGA water loss from 0 to 350 °C, calculated (found) %: 12.4 (12.6). Characteristic FT-IR-bands (cm<sup>-1</sup>): 1920 (m), 1627 (s), 1384 (w), 1359 (w), 1251 (w), 1140 (s), 1083 (s), 1022 (s), 987 (s), 938 (s), 929 (s). UV-vis bands, nm (ε): 580 (1.29 × 10<sup>3</sup>), 350 (1.65 × 10<sup>3</sup>).

$K_8Li_4[Mn^{II}_{14}(H_2O)_{26}P_8W_{48}O_{184}] \cdot 105H_2O$  (**3**). The pH of a 15 mL solution of 2 M LiCl solution was adjusted to exactly 4.0 by one drop 1 M acetic acid solution. To this solution was then added successively Mn(ClO<sub>4</sub>)<sub>2</sub> · 6H<sub>2</sub>O (102 mg, 0.28 mmol) and  $K_{28}Li_5[H_7P_8W_{48}O_{184}] \cdot 92H_2O$  (100 mg, 6.8 μmol). The very pale yellow mixture was then heated at 80 °C overnight (approximately 20 h), whereupon it turned from almost colorless to yellow, and transferred to a glass vial. The mixture was slowly cooled to room temperature and after 3 weeks of crystallizing at constant temperature (19 °C), large well-formed pale yellow plate crystals formed in solution. These were separated 7 days after crystallization began. Diffraction quality crystals were grown by the slow diffusion of methanol into the reaction mother liquor. Yield = 60 mg, 3.9 μmol, 57% based on W.

Elemental analysis for  $K_8Li_4[Mn^{II}_{14}(H_2O)_{26}P_8W_{48}O_{184}] \cdot 105H_2O$ ,  $H_{262}K_8Li_4Mn_{14}O_{315}P_8W_{48}$  (**3**), MW = 15485.68 g mol<sup>-1</sup>. Cal-

culated values (found values in brackets): Mn 4.97 (4.98), W 56.98 (56.35), K 2.02 (1.90), Li 0.18 (0.20) %.<sup>23</sup> TGA water loss from 0 to 350 °C, calculated (found) %: 12.2 (12.2). Characteristic FT-IR-bands (cm<sup>-1</sup>): 1628 (s), 1465 (w), 1319 (m), 1138 (s), 1091 (s), 1076 (s), 1020 (s), 975 (s), 959 (s), 953 (s), 936 (s), 923 (s). UV-vis bands, nm (ε): 545 (1.07 × 10<sup>3</sup>), 345 (1.75 × 10<sup>3</sup>).

**Methods. Electrochemistry.** Voltammograms were obtained using a Voltalab model GPZ 301 electro analysis system. The standard three-electrode arrangement was employed with a Pt mesh auxiliary electrode, 3 mm glassy carbon working electrode, and Ag/AgCl reference electrode. All potentials are quoted relative to the Ag/AgCl reference electrode. The glassy carbon working electrodes (diameter 3 mm) were polished with alumina (3 μm) on polishing pads and then rinsed with distilled water and sonicated in H<sub>2</sub>O and then acetone solution before each experiment. The cell was purged with Ar for at least 10 min before each experiment.

**Flame Atomic Absorption Spectroscopy (FAAS) and Flame Photometry (FP).** Analyses were performed at the Environmental Chemistry Section, School of Chemistry, The University of Glasgow on a Perkin-Elmer 1100B Atomic Absorption Spectrophotometer and A Corning Flame Photometer 410, respectively.

**Fourier-Transform Infrared (FT-IR) Spectroscopy.** The materials were prepared as KBr pellets and FT-IR spectra were collected in transmission mode using a JASCO FT-IR-410 spectrometer. Wavenumbers ( $\nu$ ) are given in cm<sup>-1</sup>; intensities as denoted as w = weak, m = medium, s = strong, br = broad, sh = sharp.

**Powder X-ray Diffraction (XRD).** Powder XRD patterns were collected on a Bruker AXS D8 powder diffractometer ( $\lambda(\text{Cu K}\alpha) = 1.5405 \text{ \AA}$ ) equipped with a graphite monochromator in capillary mode at room temperature.

**Single Crystal X-ray Diffraction.** Suitable single crystals of **2** and **3** were selected and mounted onto the end of a thin glass fiber using Fomblin oil. X-ray diffraction intensity data for both compounds were measured on an Oxford Diffraction Gemini Ultra with an ATLAS CCD detector [ $\lambda(\text{Mo K}\alpha) = 0.71073 \text{ \AA}$ ] at 150(2) K. Data reduction was performed using the CrysAlis software package, and structure solution and refinement was

(23) Our studies have shown that some metals analyzed by FAAS and FP spectroscopies often suffer from spectral interference and systematic suppression in the presence of other elements, at times as much as 5% lower than calculated values. Although the suppression of the spectroscopic profiles of the elements in compounds **2** and **3** is not significant, the data presented here do show this general trend.

carried out using SHELXS-97<sup>24</sup> and SHELXL-97<sup>25</sup> via WinGX.<sup>26</sup> Corrections for incident and diffracted beam absorption effects were applied using analytical numeric absorption correction using a multifaceted crystal model.<sup>27</sup>

**Thermogravimetric Analysis (TGA).** TGA was performed on a TA Q500 instrument under a nitrogen atmosphere. The initial heating range was from room temperature to 150 at 2.00 °C per min followed by a second range from 150 to 1000 °C at 5.00 °C per min.

**UV–vis Spectroscopy.** Solution phase UV–vis spectra and photometric studies were collected using a Shimadzu UV-3101PC

spectrophotometer in transmission mode using quartz cuvettes with 1.0 cm optical path length.

**Acknowledgment.** This work was supported by the EPSRC, BP Chemicals Ltd., WestCHEM, The Leverhulme Trust, and the University of Glasgow. We would like to thank Michael Beglan for assistance with FP and FAAS analysis. L.C. thanks the EPSRC for an Advance Fellowship and the Royal Society/Wolfson foundation for a merit award.

**Supporting Information Available:** X-ray crystallographic data in CIF format and structural figures and information on {P<sub>8</sub>W<sub>48</sub>} compounds. This material is available free of charge via the Internet at <http://pubs.acs.org>.

(24) Sheldrick, G. M. *Acta Crystallogr., Sect. A* **1990**, *46*, 467.

(25) Sheldrick, G. M. *Acta Crystallogr., Sect. A* **2008**, *64*, 112.

(26) Farrugia, L. J. *J. Appl. Crystallogr.* **1999**, *32*, 837.

(27) Clark, R. C.; Reid, J. S. *Acta Crystallogr., Sect. A* **1995**, *51*, 887.